Wavelet filtering to study mixing in 2D isotropic turbulence

Carsten Beta [a], Kai Schneider [b], Marie Farge [c],*

[a] *Fritz-Haber-Institut der Max-Planck-Gesellschaft, Faradayweg 4-6, 14195 Berlin, Germany*
[b] *Laboratoire de Modélisation et Simulation Numérique en Mecanique du CNRS & Centre de Mathématiques
et d'Informatique, Université de Provence, 39 rue Joliot-Curie, 13453 Marseille Cedex 13, France*
[c] *Laboratoire de Météorologie Dynamique, IPSL-CNRS, Ecole Normale Supérieure de Paris, 24 rue Lhomond,
75231 Paris Cedex 05, France*

Abstract

This paper presents the application of coherent vortex simulation (CVS) filtering, based on an orthogonal wavelet decomposition of vorticity, to study mixing in 2D homogeneous isotropic turbulent flows. The Eulerian and Lagrangian dynamics of the flow are studied by comparing the evolution of a passive scalar and of particles advected by the coherent and incoherent velocity fields, respectively. The former is responsible for strong mixing and produces the same anomalous diffusion as the total flow, due to transport by the coherent vortices, while mixing in the latter is much weaker and corresponds to classical diffusion.
© 2003 Elsevier B.V. All rights reserved.

1. Introduction

Decaying 2D turbulence is characterized by the emergence of long-lived coherent vortices [1]. Their dynamical properties are of primordial importance for understanding the physics of turbulence. An approach to study 2D turbulence consists in extracting coherent vortices and comparing the flow evolution, with and without them, as proposed in [2,3]. We have introduced a new method to extract coherent vortices, for 2D [4] and 3D [5] turbulent flows, which is based on an orthogonal wavelet decomposition of the vorticity field. This has lead us to develop the coherent vortex simulation (CVS) method to compute the time evolution of 2D turbulent flows [6]. The

---

* Corresponding author. Tel.: +33-1-4432-2235; fax: +33-1-4336-8392.
E-mail address: farge@lmd.ens.fr (M. Farge).

flow is decomposed into coherent components, which are computed deterministically in an adaptive wavelet basis, and incoherent random components, which are discarded and whose effect is statistically modelled. In the present work, we analyze the time evolution of a decaying 2D homogeneous isotropic turbulent flow, by applying the CVS filtering at each time step of a Direct Numerical Simulation (DNS). We compare the Eulerian and Lagrangian mixing properties of the total, the coherent, and the incoherent flows during several eddy turn-over times.

2. Physical problem and numerical method

We consider a two-dimensional incompressible and Newtonian flow governed by the Navier–Stokes equations,

$$\partial_t \omega + (\mathbf{v} \cdot \nabla)\omega - \nu \nabla^2 \omega = 0 \quad \text{and} \quad \nabla \cdot \mathbf{v} = 0, \tag{1}$$

with velocity $\mathbf{v} = (u, v)$, vorticity $\omega = \nabla \times \mathbf{v}$, and kinematic viscosity $\nu = 9.9 \times 10^{-4}$ m²/s, which corresponds to a Reynolds number $Re = 1236$, based on the kinetic turbulent energy and the size of the domain. The boundary conditions are periodic and the initial conditions correspond to a fully developed turbulent flow previously computed [4]. The eddy turnover time, $\tau = 1/\sqrt{2Z(0)} = 0.5$ s, is based on the initial enstrophy $Z(0)$ with $Z = (1/2)\langle \omega, \omega \rangle$, where $\langle \cdot, \cdot \rangle$ denotes the L^2-inner product. The DNS is performed using a classical pseudo-spectral method with resolution $N = 256^2 = 2^{2J}$ with $J = 8$, and a semi-implicit time integration with $\Delta t = 5 \times 10^{-4}$ s.

The CVS filtering is applied at each time step. For that the vorticity field $\omega^n(x, y)$ is projected onto an orthogonal wavelet basis ψ^μ_{j,i_x,i_y}, where j denotes the scale, i_x and i_y the two space coordinates, and μ the three spatial directions (vertical, horizontal, and diagonal). We choose orthogonal spline wavelets of order six, which constitute a 2D multi-resolution analysis [7]. The N wavelet coefficients $\widetilde{\omega}^\mu_{j,i_x,i_y} = \langle \omega, \psi^\mu_{j,i_x,i_y} \rangle$, for $j = 0, \ldots, J - 1$, $i_x, i_y = 0, \ldots, 2^j - 1$, and $\mu = 1, 2, 3$, are computed with the fast wavelet transform [7]. Subsequently, they are split into coherent contributions, which correspond to those coefficients whose modulus $|\widetilde{\omega}^\mu_{j,i_x,i_y}|$ is larger than a given threshold ϵ_T, and incoherent contributions, which correspond to the remaining weaker wavelet coefficients. The threshold is defined as $\epsilon_T = 2(Z \log_e N)^{1/2}$, where Z is the total enstrophy and N the resolution. The choice of ϵ_T is based on theorems by Donoho & Johnstone [8] proving the optimality of the wavelet representation to obtain min–max estimators for denoising of signals with inhomogeneous regularity. The coherent and incoherent vorticity fields, ω_C and ω_I respectively, are reconstructed by inverse wavelet transform, yielding $\omega = \omega_C + \omega_I$. The corresponding coherent and incoherent velocity fields, $\mathbf{v}_C$ and $\mathbf{v}_I$ respectively, are computed using the Biot–Savart's enstrophy law, $\mathbf{v} = \nabla^\perp(\nabla^{-2}\omega)$, yielding $\mathbf{v} = \mathbf{v}_C + \mathbf{v}_I$. Note that this decomposition is orthogonal for vorticity, $Z = Z_C + Z_I$, but only approximately orthogonal for velocity, $E = E_C + E_I + \varepsilon$ with $\varepsilon \ll E = (1/2)\langle \mathbf{v}, \mathbf{v} \rangle$.

3. Results

In the column on the left hand side of Fig. 1, three snapshots of the time evolution of the vorticity field are displayed as they are computed from DNS. The corresponding coherent and
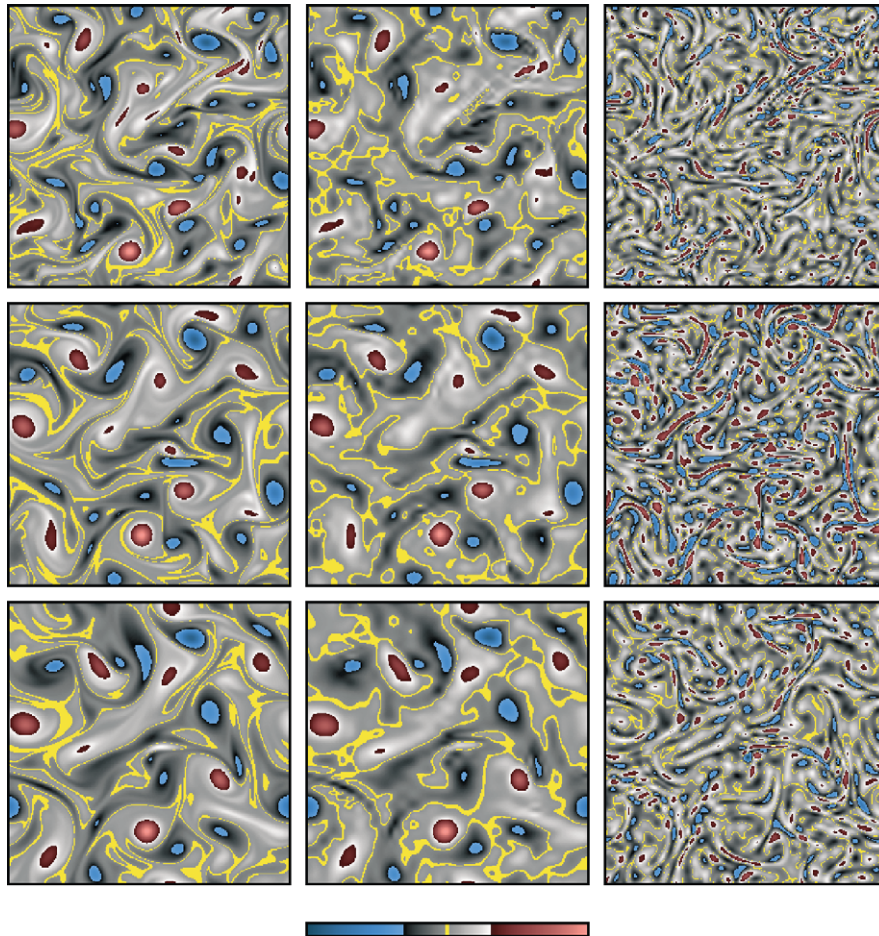
Fig. 1. Time evolution of the total (left), the coherent (middle), and the incoherent (right) vorticity fields. The snapshots are taken at $t = 0\tau$ (top), $t = 5\tau$ (middle), and $t = 10\tau$ (bottom).

incoherent parts are shown in the middle and right hand column, respectively. The coherent flow is represented by only 0.8% N wavelet modes which retain 99% of the energy and 85% of the enstrophy. Furthermore, it shows the same probability distribution function (PDF) of vorticity (Fig. 3), the same energy spectrum in the inertial range (Fig. 4), and the same spatial distribution of coherent vortices as the total flow (compare the left and middle columns of Fig. 1). In contrast, the incoherent flow, represented by the remaining 99.2% N wavelet modes, is made of only weak vorticity filaments. It exhibits a Gaussian vorticity PDF (Fig. 3) and an enstrophy equipartition spectrum close to k^{+1}, k being the modulus of the wavenumber, which corresponds to an energy spectrum in k^{-1} (Fig. 4).

The evolution of a passive scalar field $\theta(\mathbf{x}, t)$ (e.g., temperature or concentration) follows the advection–diffusion equation

$$\partial_t \theta + (\mathbf{v} \cdot \nabla)\theta - \kappa \nabla^2 \theta = 0, \tag{2}$$
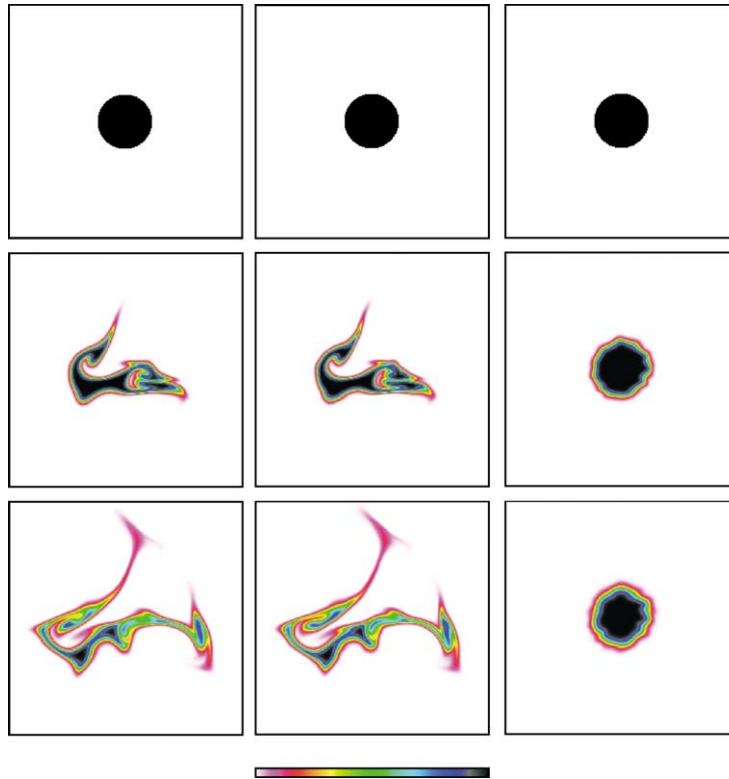
Fig. 2. Advection–diffusion process of a passive tracer in the total (left), coherent (middle), and incoherent (right) flows. The snapshots are taken at $t = 0\tau$ (top), $t = 5\tau$ (middle), and $t = 10\tau$ (bottom).
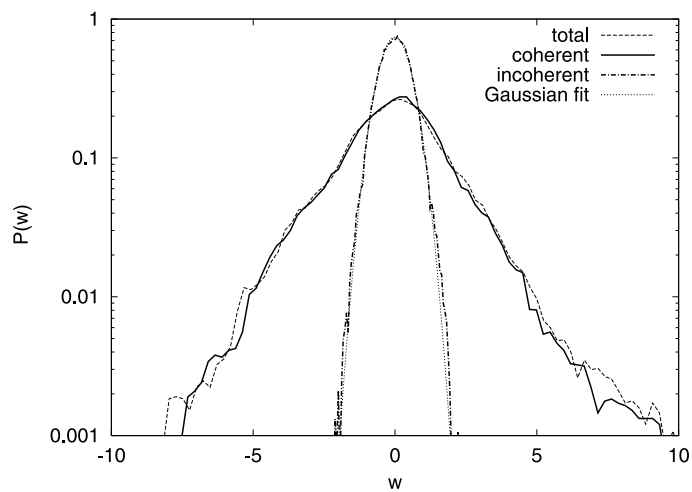
Fig. 3. Vorticity PDFs of the total, coherent, and incoherent flows at $t = 0$.
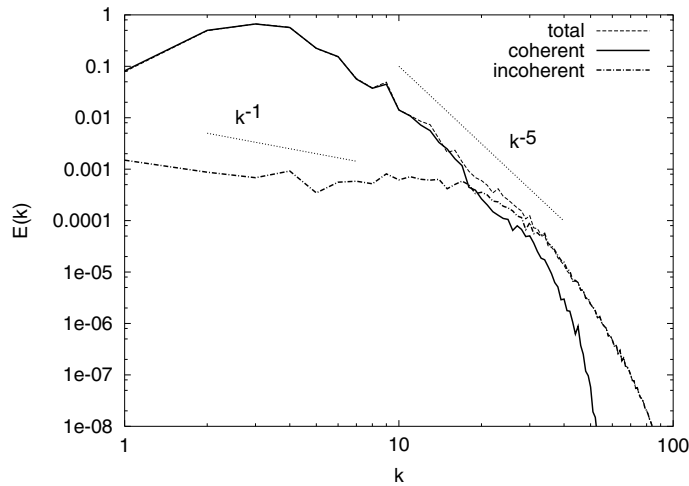
Fig. 4. Energy spectra of the total, coherent, and incoherent flows at $t = 0$.

where κ denotes the molecular diffusivity. As initial condition we choose a circular spot of tracer with a diameter corresponding to one quarter of the computational domain. We consider a tracer with Schmidt number $Sc = v/\kappa = 1$, whose concentration has been normalized between zero and one. Using a pseudo-spectral method, we solve the advection–diffusion equation three times, with the total velocity $\mathbf{v}$, the coherent velocity $\mathbf{v}_C$, and the incoherent velocity $\mathbf{v}_I$. In Fig. 2, three snapshots of the advection–diffusion process of the passive scalar are shown for the time evolution in the total flow (left) parts as well as for the evolution in the coherent (middle) and incoherent (right) parts. From comparison of the left and middle columns in Fig. 2, it becomes obvious that mixing of the passive scalar by the coherent flow alone (middle) is similar to the one by the total flow (left). For both the total and the coherent flows we observe characteristic stretchings and foldings of the tracer spot, which tend to maximize the length of the interface between mixed and unimixed regions. They are responsible for the production of scalar gradients (Fig. 5), $\Gamma(t) = \int \gamma(\mathbf{x}, t)\, d\mathbf{x}$, where the local scalar gradient production, $\gamma = \frac{1}{2}|\nabla\theta|s\cos 2\alpha$, is proportional to the cosine of the angle α between the scalar gradient vector and the compressing eigenvector of the strain tensor, $s = \sqrt{s_{11}^2 + s_{12}^2}$ with $s_{11} = \partial_x u - \partial_y v$ and $s_{12} = \partial_x v + \partial_y u$ [9]. Moreover, for both the total and the coherent flows, the concentration fields present the same time evolution for the difference between their variances $\sigma = \langle(\theta - \bar{\theta})^2\rangle$ at time t and at initial time $t = 0$ (Fig. 6). At the beginning, we observe a purely diffusive behaviour, $(\sigma(0) - \sigma(t)) \propto t^{1/2}$ which evolves at later times towards an accelerated anomalous diffusion, $(\sigma(0) - \sigma(t)) \propto t$. In contrast, the effect of the incoherent flow on the passive scalar is different and remains purely diffusive, since the difference between the scalar variances $(\sigma(t) - \sigma(0))$ evolves in $t^{1/2}$ (Fig. 6) [10]. The scalar spot is neither stretched nor distorted (Fig. 2, right) and there is no production of scalar gradients (Fig. 5) by the incoherent flow.

Finally, we study the time evolution of point particles advected by the total, the coherent, and the incoherent flows, respectively. This corresponds to the advection–diffusion of a passive scalar with infinite Schmidt number (i.e., $\kappa = 0$). Fig. 7 shows that the particle trajectories are similar for the total and coherent flows, where curved trajectories correspond to particles trapped by vortices,
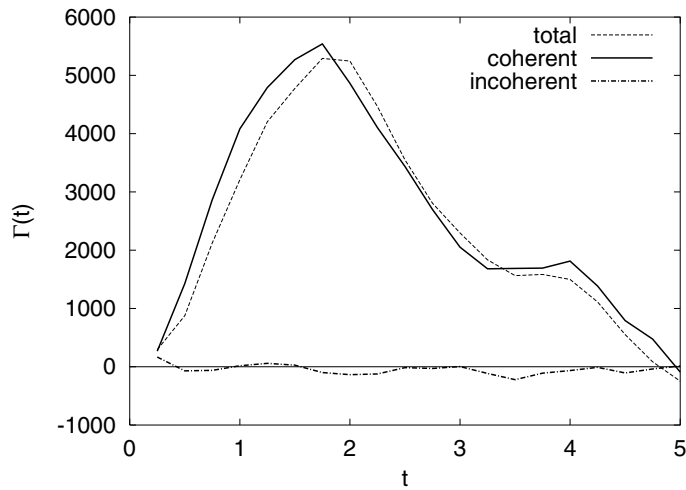
Fig. 5. Production of scalar gradients for the mixing process in the total, coherent, and incoherent flows.
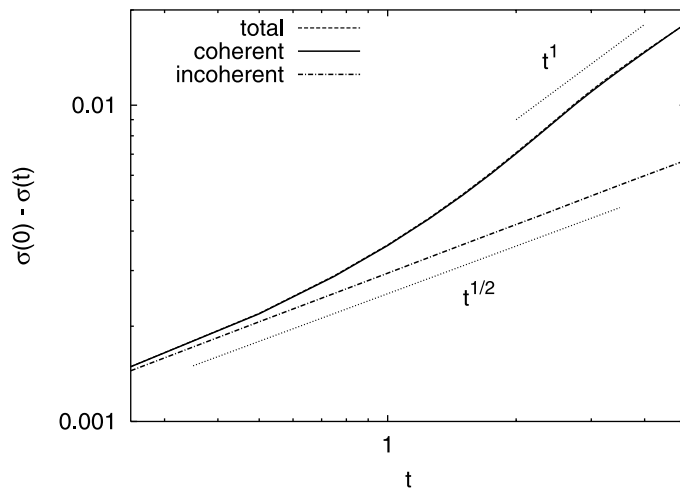
Fig. 6. Evolution of the difference between initial and instantaneous scalar variances for the mixing process in the total, coherent, and incoherent flows.
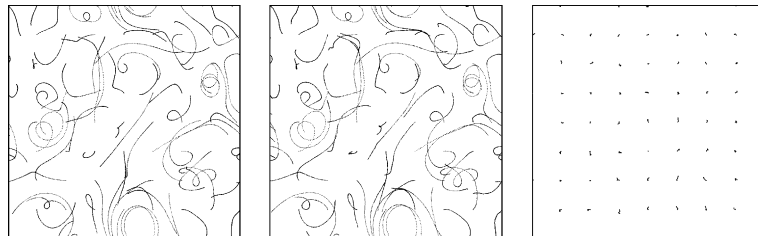
Fig. 7. Particle trajectories from $t = 0$ to 10τ in the total (left), coherent (middle), and incoherent (right) flows.

and straight trajectories to free flights between vortices. We compute one- and two-point Lagrangian statistics averaged over 1024 trajectories. The PDFs of the Lagrangian velocities are Gaussian distributions, and very similar to the PDFs of the Eulerian velocities (Fig. 8). The PDFs of the total and coherent velocities superimpose almost perfectly, while the PDF of the incoherent velocity has a strongly reduced variance (Fig. 8). The energy spectra of all the Lagrangian velocities show a power law behaviour, $E^L(f) \propto f^{-2}$, f being the time frequency (Fig. 9). For small and large f, however, the spectrum of the incoherent velocity differs from those of the coherent and total velocities, which are almost identical. Computing their inverse Fourier transforms we obtain the Lagrangian velocity autocorrelation functions, $R^L(t) = \langle v(t')v(t'+t)\rangle_{t'}/\langle v^2\rangle$ plotted in the inset of Fig. 10. For the incoherent flow we can identify an exponential behaviour, $R^L(t) \propto \exp(-t/T^L)$, which corresponds to a Lorentzian form of the spectrum, $E^L(f) = \langle v^2\rangle T^L/[1 + (T^L f)^2]$ [11], where $T^L = \int_0^\infty R^L(t)\,dt$ is the integral time scale. For the total and
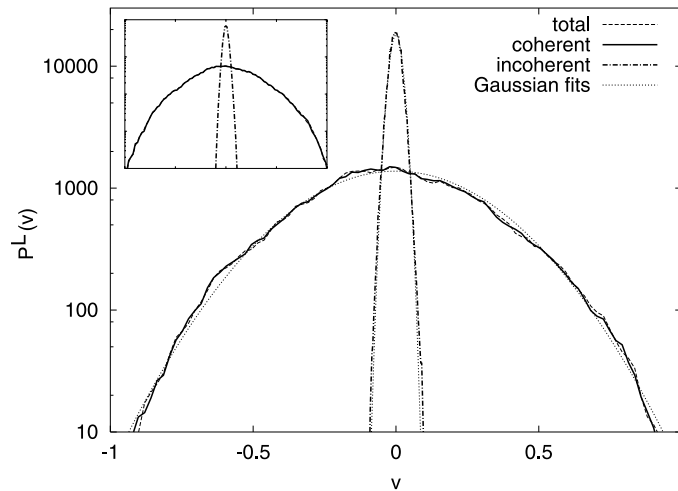
Fig. 8. PDF of the total, coherent, and incoherent Lagrangian velocities (Inset: PDF of the Eulerian velocities).
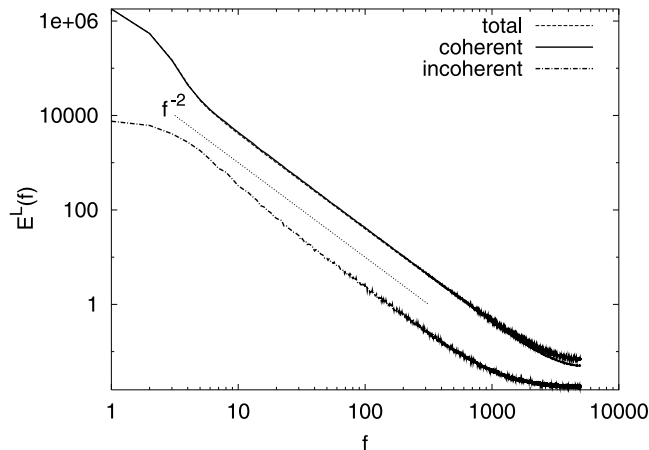
Fig. 9. Energy spectra of the total, coherent, and incoherent Lagrangian velocities.
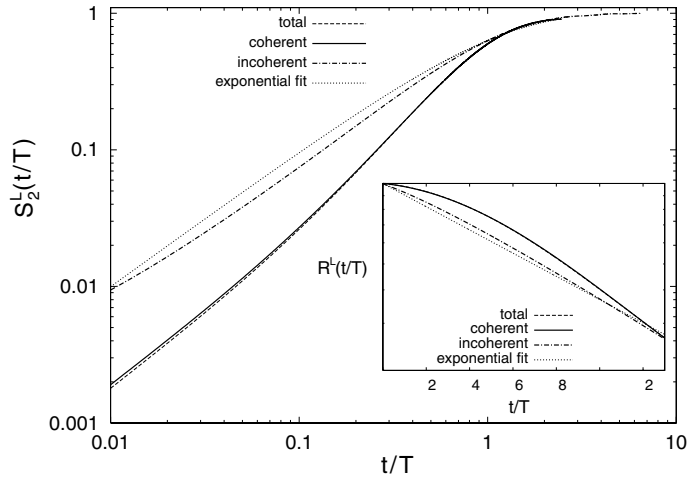
Fig. 10. Second order structure functions as function of the nondimensionalized time t/T^L (inset: corresponding velocity autocorrelation functions).

coherent flows R^L are almost identical and depart from exponential decay (inset Fig. 10) with a correlation time ($T^L_{tot} = T^L_{coh} = 0.81\tau$) which is 2.6 times longer than for the incoherent flow ($T^L_{inc} = 0.31\tau$). Finally, the second order structure function of the Lagrangian velocity increments, $S^L_2(t) = \langle |v(t'+t) - v(t')|^2 \rangle_{t'} / (2\langle v^2 \rangle)$, scales linearly in t for the incoherent flow (Fig. 10). For the total and coherent flows we only see the same behaviour for very small t, while they both progressively increase towards a t^2 behaviour. In all cases, $S^L_2(t)$ saturates at 1 as $v(t')$ and $v(t'+t)$ become uncorrelated for large t.

4. Conclusion

We have shown that the coherent flow is responsible for the transport of passive scalar and of particles causing anomalous diffusion and strong mixing. The incoherent flow has only a purely diffusive effect, similar to a Brownian motion, which results in classical diffusion and much weaker mixing. This suggests to model the influence of the incoherent velocity using simple Langevin-like stochastic equations. These results confirm that the CVS filtering, based on a nonlinear thresholding of the vorticity in wavelet space, disentangles different dynamical behaviours of 2D turbulent flows, namely transport by nonlinearly interacting coherent vortices and diffusion by an incoherent background flow. Our conjecture is that the observations made here for 2D turbulent flows are also true in 3D, since we have shown [5,6] that CVS filtering keeps its efficiency to extract coherent vortices in 3D turbulent flows.

References

[1] McWilliams J. The emergence of isolated coherent vortices in turbulent flow. J Fluid Mech 1984;146:21–43.

[2] Benzi R, Patarnello S, Santangelo P. Self-similar coherent structures in two-dimensional decaying turbulence. J Phys A Math Gen 1988;21:1221–37.

[3] Babiano A, Basdevant C, Legras B, Sadourny R. Vorticity and passive-scalar dynamics in two-dimensional turbulence. J Fluid Mech 1987;183:379–97.

[4] Farge M, Schneider K, Kevlahan N. Non-gaussianity and coherent vortex simulation for two-dimensional turbulence using an adaptive orthogonal wavelet basis. Phys Fluids 1999;11:2187–201.

[5] Farge M, Pellegrino G, Schneider K. Coherent vortex extraction in 3d turbulent flows using orthogonal wavelets. Phys Rev Lett 2001;87:054501.

[6] Farge M, Schneider K. Coherent vortex simulation (CVS): a semi-deterministic turbulence model. Flow Turbul Combust 2001;66:393–426.

[7] Farge M. Wavelet transforms and their applications to turbulence. Annu Rev Fluid Mech 1992;24:395.

[8] Donoho D, Johnstone I. Ideal spatial adaptation by wavelet shrinkage. Biometrika 1994;81:425–55.

[9] Protas B, Babiano A, Kevlahan N. On geometrical alignment properties of two-dimensional forced turbulence. Physica D 1999;128:169–79.

[10] Flohr P, Vassilicos J. Accelerated scalar dissipation in a vortex. J Fluid Mech 1997;348:295–317.

[11] Pope S. Turbulent flows. Cambridge: Cambridge University Press; 2000.